

# Terahertz electromagnetic crystal waveguide fabricated by polymer jetting rapid prototyping

Ziran Wu,<sup>1,2</sup> Wei-Ren Ng,<sup>2</sup> Michael E. Gehm,<sup>2,3</sup> Hao Xin<sup>1,2,\*</sup>

<sup>1</sup>Department of Physics, University of Arizona, Tucson AZ 85719, USA

<sup>2</sup>Department of Electrical and Computer Engineering, University of Arizona, Tucson AZ 85721, USA

<sup>3</sup>College of Optical Science, University of Arizona, Tucson AZ 85721, USA

\*hxin@ece.arizona.edu

**Abstract:** An all-dielectric THz waveguide has been designed, fabricated and characterized. The design is based on a hollow-core electromagnetic crystal waveguide, and the fabrication is implemented via polymer-jetting rapid prototyping. Measurements of the waveguide power loss factor show good agreement with simulation. As an initial example, a waveguide with propagation loss of 0.03 dB/mm at 105 GHz is demonstrated.

© 2011 Optical Society of America

**OCIS codes:** (050.5298) Photonic crystals; (130.5460) Polymer waveguides; (260.3090) Infrared, far; (050.6875) Three-dimensional fabrication; (220.4000) Microstructure fabrication.

---

## References and links

1. P. H. Siegel, "Terahertz Technology," *IEEE Trans. Microw. Theory Tech.* **50**(3), 910–928 (2002).
2. S. Atakaramians, S. V Afshar, B. M. Fischer, D. Abbott, and T. M. Monro, "Porous fibers: a novel approach to low loss THz waveguides," *Opt. Express* **16**(12), 8845–8854 (2008).
3. C. D. Nordquist, M. C. Wanke, A. M. Rowen, C. L. Arrington, M. Lee, and A. D. Grine, "Design, fabrication, and characterization of metal micromachined rectangular waveguides at 3 THz," in *IEEE AP-S Int. Symp.* (San Diego, CA, 2008), pp. 1–4.
4. T. Ito, Y. Matsuura, M. Miyagi, H. Minamide, and H. Ito, "Flexible Terahertz fiber optics with low bend-induced losses," *J. Opt. Soc. Am. B* **24**(5), 1230–1235 (2007).
5. R. Mendis, and D. Grischkowsky, "Undistorted guided-wave propagation of subpicosecond terahertz pulses," *Opt. Lett.* **26**(11), 846–848 (2001).
6. K. Wang, and D. M. Mittleman, "Metal wires for terahertz wave guiding," *Nature* **432**(7015), 376–379 (2004).
7. T.-I. Jeon, J. Zhang, and K. W. Goossen, "THz Sommerfeld wave propagation on a single metal wire," *Appl. Phys. Lett.* **86**(16), 161904 1–3 (2005).
8. T.-I. Jeon, and D. Grischkowsky, "Direct optoelectronic generation and detection of sub-ps-electrical pulses on sub-mm-coaxial transmission lines," *Appl. Phys. Lett.* **85**(25), 6092–6094 (2004).
9. L.-J. Chen, H.-W. Chen, T.-F. Kao, J.-Y. Lu, and C.-K. Sun, "Low-loss subwavelength plastic fiber for Terahertz waveguiding," *Opt. Lett.* **31**(3), 308–310 (2006).
10. A. Dupuis, J.-F. Allard, D. Morris, K. Stoeffler, C. Dubois, and M. Skorobogatiy, "Fabrication and THz loss measurements of porous subwavelength fibers using a directional coupler method," *Opt. Express* **17**(10), 8012–8028 (2009).
11. S. Atakaramians, S. V. Afshar, H. Eboroff-Heidepriem, M. Nagel, B. M. Fischer, D. Abbott, and T. M. Monro, "THz porous fibers: design, fabrication and experimental characterization," *Opt. Express* **17**(16), 14053–15062 (2009).
12. M. Goto, A. Quema, H. Takahashi, S. Ono, and N. Sarukura, "Teflon photonic crystal fiber as Terahertz waveguide," *Jpn. J. Appl. Phys.* **43**(2B 2B), L317-L319 (2004).
13. K. Nielsen, H. K. Rasmussen, A. J. L. Adam, P. C. M. Planken, O. Bang, and P. U. Jepsen, "Bendable, low-loss Topas fibers for the terahertz frequency range," *Opt. Express* **17**(10), 8592–8601 (2009).
14. J.-Y. Lu, C.-P. Yu, H.-C. Chang, H.-W. Chen, Y.-T. Li, C.-L. Pan, and C.-K. Sun, "Terahertz air-core microstructure fiber," *Appl. Phys. Lett.* **92**(6), 064105 1–3 (2008).
15. M. Skorobogatiy, and A. Dupuis, "Ferroelectric all-polymer hollow Bragg fibers for terahertz guidance," *Appl. Phys. Lett.* **90**(11), 1135141–1135143 (2007).
16. W. R. McGrath, C. W. Walker, M. Yap, and Y.-C. Tai, "Silicon micromachined waveguides for millimeter-wave and submillimeter-wave frequencies," *IEEE Microwave Guided Wave Lett.* **3**(3), 61–63 (1993).
17. J. W. Digby, C. E. McIntosh, G. M. Parkhurst, and S. R. Davies, "Fabrication and characterization of micromachined rectangular components for use at millimeter and terahertz frequencies," *IEEE Trans. Microw. Theory Tech.* **48**(8), 1293–1302 (2000).
18. J. D. Joannopoulos, S. G. Johnson, J. N. Winn, and R. D. Meade, *Photonic crystals: Molding the flow of Light*, 2nd ed. (Princeton University Press, Princeton, NJ, 2008).
19. Z. Wu, J. Kinast, M. E. Gehm, and H. Xin, "Rapid and inexpensive fabrication of terahertz electromagnetic bandgap structures," *Opt. Express* **16**(21), 16442–16451 (2008).

20. C. E. Honingh, M. M. Dierichs, H. H. Schaeffer, T. M. Klapwijk, and Th. de Graauw, "A 345 GHz waveguide mixer using an array of four Nb-Al-Al<sub>2</sub>O<sub>3</sub>-Nb SIS junctions," *Supercond. Sci. Technol.* **4**(11), 683–685 (1991).
21. K. Yamamoto, M. Yamaguchi, F. Miyamaru, M. Tani, M. Hangyo, T. Ikeda, A. Matsushita, K. Koide, M. Tatsuno, and Y. Minami, "Noninvasive inspection of C-4 explosive in mails by terahertz time-domain spectroscopy," *Jpn. J. Appl. Phys.* **43**(3B 3B), L414–L417 (2004).
22. Z. Wu, W.-R. Ng, M. Gehm, and H. Xin, "Hollow-core electromagnetic band gap (EBG) waveguide fabricated by rapid prototyping for low-loss Terahertz guiding," in *IEEE MTT-S Int. Microwave Symp.* (Anaheim, CA, 2010).
23. Z. Wu, W.-R. Ng, M. Gehm, and H. Xin, "Terahertz electromagnetic crystal (EMXT) based waveguide and horn antenna," in *35th Int. Conf. on Infrared, Millimeter and Terahertz Waves*, (Rome, Italy, 2010).
24. B. Martinez, I. Ederra, R. Gonzalo, B. Alderman, L. Azcona, P. G. Huggard, B. D. Hon, A. Hussain, S. R. Andrews, and L. Marchand, "Manufacturing tolerance analysis, fabrication, and characterization of 3-D submillimeter-wave electromagnetic-band gap crystals," *IEEE Trans. Microw. Theory Tech.* **55**(4), 672–681 (2007).
25. V. M. Lubecke, K. Mizuno, and G. M. Rebeiz, "Micromaching for Terahertz applications," *IEEE Trans. Microw. Theory Tech.* **46**(11), 1821–1831 (1998).
26. R. Gonzalo, B. Martinez, C. M. Mann, H. Pellemans, P. H. Bolivar, and P. de Maagt, "A low-cost fabrication technique for symmetrical and asymmetrical layer-by-layer photonic crystals at submillimeter-wave frequencies," *IEEE Trans. Microw. Theory Tech.* **50**(10), 2384–2392 (2002).
27. E. Öbay, E. Michel, G. Tuttle, R. Biswas, K. M. Ho, J. Bostak, and D. M. Bloom, "Terahertz spectroscopy of three-dimensional photonic bandgap crystals," *Opt. Lett.* **10**(15), 1155–1157 (1994).
28. F. Laermer, and A. Urban, "Challenges, developments and applications of silicon deep reactive ion etching," *Microelectron. Eng.* **67–68**(1), 349–355 (2003).
29. G. Kiriakidis, and N. Katsarakis, "Fabrication of 2-D and 3-D photonic band-gap crystals in the GHz and THz regions," *Mater. Phys. Mech.* **1**, 20–26 (2000).
30. S. G. Johnson, and J. D. Joannopoulos, "Block-iterative frequency-domain methods for Maxwell's equations in a planewave basis," *Opt. Express* **8**(3), 173–190 (2001).
31. Lumerical MODE Solutions package, v2.3.
32. P. F. Goldsmith, *Quasioptical systems: Gaussian beam quasioptical propagation and applications* (IEEE Press, Piscataway, NJ, 1997).
33. W.-H. Yu, Y.-J. Liu, T. Su, H. Neng-Tien, and M. Raj, "A robust parallel conformal finite difference time domain processing package using MPI library," *IEEE Ant. Propag. Mag.* **47**(3), 39–59 (2005).
34. G. Gruner, ed., *Millimeter and Submillimeter Wave Spectroscopy of Solids* (Springer, Berlin, German, 1998).
35. J. C. Daly, *Fiber Optics* (CRC Press, Boca Raton, Florida, 2000).

## 1. Introduction

Research involving the Terahertz (THz) spectrum (100 GHz–10 THz) has experienced dramatic growth recently in both technical achievement and commercial implementation. The growth is application driven, with interest from various fields such as chemical and astronomical spectroscopy and sensing, medical and biological imaging and analysis, defense and security screening, communication networks and radars, etc [1]. Many of these applications, however, utilize free-space propagation, resulting in weak beam confinement and vulnerability to environmental fluctuations. Focal spot size is diffraction limited and relatively large for the wavelengths of interest [2], which inconveniently requires large sample areas in material characterization applications and makes system miniaturization challenging. THz waveguides, on the other hand, provide a promising approach to overcome these drawbacks, and may lead to compact and low-cost integrated THz systems.

Various types of THz waveguides based on both electronic and photonic technologies have been proposed and studied, including metallic rectangular/circular [3, 4], parallel-plate [5], metal wire [6, 7], coaxial transmission line [8], sub-wavelength fiber [2, 9–11], photonic crystal fiber (PCF) [12–15], etc. However, realization of a THz waveguide with acceptable performance remains a challenge in many regards such as loss, cost, coupling, and especially fabrication and component integration. For most of the reported THz waveguides, fabrication usually involves either photolithography/micromachining work flows [3–5, 14, 16, 17] or high-temperature and hazardous hot-draw or CVD processes [10, 12, 13, 15]. Several of the demonstrated waveguides also required hand assembly [12, 14], which compromises fabrication accuracy and prohibits large scale production. Moreover, integration with other components or variation in waveguide parameters within a single piece of guide remains to be challenging.

In this paper, an all-dielectric waveguide operating near 112 GHz is designed and demonstrated. The waveguide is based on a hollow-core electromagnetic crystal (EMXT)

structure [18]. Both eigen-mode and driven-mode simulations are performed to verify its power transmission spectrum and propagation loss. Fabrication of the waveguide is via a novel polymer-jetting rapid prototyping technique [19]. Due to the layer-by-layer printing nature of this technique, the fabrication is very convenient, accurate, mass-production capable, and highly flexible. Several waveguides of identical cross-section and various lengths were fabricated to enable THz time-domain spectroscopy characterization of the intrinsic power loss factor. Measurement results agree well with simulation, exhibiting a low power loss of 0.03 dB/mm at 105 GHz. This waveguide is quite suitable for narrow-band applications, including space and earth science spectroscopy at atmospheric window frequencies such as 94 GHz and 345 GHz [1, 20], as well as screening and imaging applications of chemical or biological agents at their signature frequencies [1], such as commonly used explosives at 807 GHz [21]. Moreover, under the scope of the same prototyping fabrication technique, the waveguide aperture can be easily expanded to form an electromagnetic crystal horn antenna, which would greatly enhance the coupling to THz free-space radiation [22, 23]. With proper transition structure from the waveguide to planar circuits, solid-state sources and detectors may be integrated with the waveguide and horn antenna to realize compact THz transceiving systems. Therefore, this waveguide serves as a critical building block in potential integrated THz systems that can be readily implemented by the proposed polymer-jetting rapid prototyping technique.

## 2. Polymer jetting rapid prototyping

THz electromagnetic crystal and associated components fabrication is still a major challenge remaining to be overcome, as the feature dimensions of THz EMXT components fall in a transition region between the conventional micromachining techniques used for microwave applications and the micro/nano-fabrication methods in use at optical frequencies [24, 25]. Several semiconductor fabrication approaches, including dicing saw machining (with minimum feature size reaching 25  $\mu\text{m}$ ) [26], wet etching (able to define  $\sim 50$   $\mu\text{m}$  features) [27], deep reactive ion etching (DRIE) (gaps of several  $\mu\text{m}$  width and  $\sim 10$   $\mu\text{m}$  height demonstrated) [28], deep X-ray lithography (tens of micron fabrication resolution) [29] and laser micromachining (below 10  $\mu\text{m}$  feature size, depending on the laser spot size) [24, 29], have been reported. For THz micro-structured or porous fiber fabrication, hot-drawn method is generally employed, with the fiber preform prepared by various methods including stacking [14], drilling [13] and die extrusion [11]. The achieved cross-section feature size for the hot-drawn method is usually on the order of 100  $\mu\text{m}$ .

Previously, we have demonstrated fabrication of THz electromagnetic crystal structures via polymer-jetting rapid prototyping [19]. This fabrication process is quite straightforward. The 3-D geometry of a THz structure is imported into a CAD program and converted into a series of layered slices, each representing a 16- $\mu\text{m}$  thick region of the structure in the  $z$  dimension. The slice description consists of two different material types — a model material which is assigned to regions that are part of the structure cross-section, and a water soluble support material that fills all other regions and provides a base upon which the model sections of future slices can rest. The data set describing the slices is sent sequentially to the prototyping machine. A series of print heads, similar to those on an inkjet printer, deposit a thin layer of ultraviolet (UV)-curable polymer onto the construction tray. UV lamps on the print head immediately cure materials as they are being deposited. Once the layer is completed, the construction tray is lowered by 16  $\mu\text{m}$  and the next slice is processed. After the whole model is printed, the support material is washed away using a high-pressure water spray, and the structure is cleaned and ready for testing and applications. The minimum practical feature size in  $x$  and  $y$  dimensions is founded to be 100~150  $\mu\text{m}$  despite the stated printing resolution of 42  $\mu\text{m}$  of the printer. Nevertheless, THz wavelength features can be well realized with these prototyping resolutions. The printer also includes a “glossy” mode that preferentially minimizes the amount of support material and produces correspondingly smoother model surfaces as a result.

Several 3-D THz electromagnetic crystal components have been successfully fabricated by this method [19]. Excellent agreement between simulated and measured THz responses of these components validated the accuracy and fabrication flexibility of this method while simultaneously demonstrating its high-speed and low-cost nature. Advanced extensions to this technique, including systematic integration of various THz components (e.g. antennas, filters and power dividers) and metallization of finished components are currently being explored as possible routes to integrated THz systems.

### 3. Electromagnetic crystal waveguide design

The waveguide structure of interest is based on a central air core channel in a surrounding triangular-lattice of air cylinders in a dielectric background. Because of the Bragg diffraction in the lattice, this structure exhibits electromagnetic band gaps in certain frequency bands. Within the band gaps, wave propagation is prohibited and therefore the structure is able to confine the wave propagation. If an air channel is present, this structure will support wave propagation along the channel in the band gap frequency, whereas the radiation loss along the propagation path will be greatly suppressed because of the electromagnetic band gap cladding. More importantly, the wave suffers much less loss than in conventional optical fiber because the majority of the power propagates in the central air-filled channel [18]. Therefore, this type of waveguides is promising as a route to achieving extremely low transmission loss.

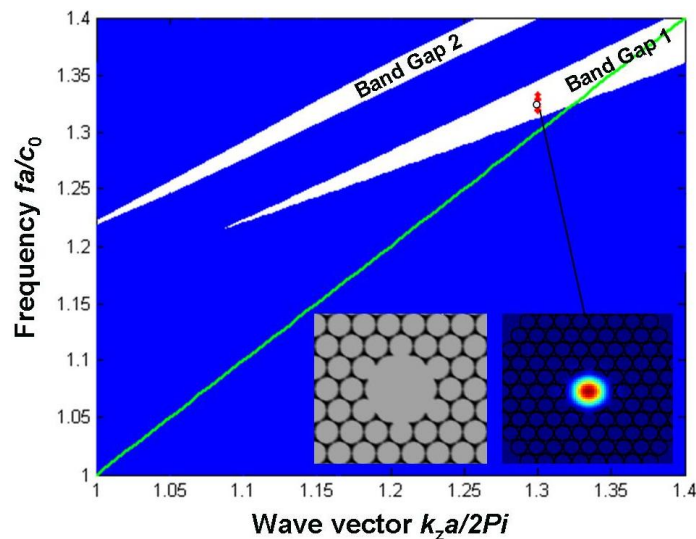


Fig. 1. Band diagram of the complete electromagnetic crystal lattice and the hollow-core waveguide modes. For the electromagnetic crystal lattice, dark (blue online) regions denote the continuous modes region whereas in white regions no mode exists (band gaps). Inset (left) shows the schematic of the waveguide cross section when a center air core channel is introduced. Waveguide modes are marked by the dots (red) in the “Band Gap 1” region, among which the energy intensity profile of the fundamental  $HE_{11}$  mode is shown in the inset (right).

#### 3.1 Eigen-mode simulations

Figure 1 is the band diagram of the complete electromagnetic crystal lattice with hollow-core waveguide mode marked, calculated using the MIT Photonic Bandgap package (MPB) which utilizes a plane-wave expansion method [30]. Dark (blue online) regions on the band diagram consist of continuous modes of the electromagnetic crystal lattice. White regions denote where no modes exist, therefore opening several band gaps. As shown in the leftmost inset, a triangular-lattice arrangement of small air cylinders (grey) are embedded in a dielectric background (black) with dielectric constant of 2.75. An air channel is present at the center. The cladding cylinders have a radius of  $0.47a$  with  $a$  being the lattice constant, and the air core has a radius of  $1.4a$ . This channel results in a number of waveguide modes within the

band gaps of the complete electromagnetic crystal lattice, as denoted by the dots (red online) in Fig. 1. Note that only modes beyond the light line (green online) are capable of propagation. As the band gap of the cladding rings suppresses propagation transverse to the axis, these waveguide modes create efficient energy confinement and propagation along the central core.

The rightmost inset of the figure shows the energy distribution of the fundamental  $HE_{11}$  mode within the first electromagnetic band gap, obtained from an effective-index-based eigen-mode simulation using the Lumerical MODE Solutions package [31]. The MPB simulation reveals that approximately 91% of the energy is concentrated within the central channel for this propagating mode, with an intensity profile following approximately Gaussian distribution. A simple mode-matching argument then indicates that efficient excitation of this propagating mode should be achievable with an incident, linearly-polarized Gaussian beam [32].

The waveguide design is scalable in frequency as the normalized axis of the band diagram in Fig. 1 illustrates. In the practical design considered here, a lattice constant of 3 mm is used, resulting in a center core radius of 4.2 mm. The cladding air cylinder radius is slightly reduced to 1.3 mm. The dielectric wall thickness between air cylinders is then 400  $\mu\text{m}$  at its thinnest, providing reasonable mechanical robustness for the initial trial. The dielectric properties of the polymer used in the rapid prototyping process was previously characterized by THz time-domain spectroscopy in our earlier work. From that study, we observed that it has a dielectric constant of 2.75 and loss tangent of 0.02 near 150 GHz [19]. Using these properties, the simulated operating frequency of the fundamental  $HE_{11}$  mode is approximately 112 GHz. With these practical design parameters, the intrinsic radiation loss of the  $HE_{11}$  mode at 112 GHz (ignoring the material loss) was calculated to be 0.012 dB/mm using Lumerical MODE Solutions.

### 3.2 Driven mode simulations

In order to estimate the overall propagation loss of the waveguide design including the material loss and effects from other higher-order modes, we then simulated the waveguide under two different excitations, using a finite-difference- time-domain based package (GEMS [33]). The first excitation employed two circular perfect-electric-conductor waveguide feeds inserted into the dielectric waveguide apertures at both ends. Two wave ports excited the  $TE_{11}$  mode in the feeds, which then propagated through an 84-mm long electromagnetic crystal waveguide.

Figure 2 depicts the resulting S-parameters. Four passbands are observed around 112, 130, 161 and 182 GHz, corresponding to the band gaps of the original electromagnetic crystal lattice. The field profile in the waveguide at 112 GHz resembles the desired  $HE_{11}$  mode as shown in Fig. 1. The 3-dB bandwidth of the first passband centered at 112 GHz is about 15.8 GHz, giving a full bandwidth to mid-gap frequency ratio of 14.1%. The reflection coefficient  $S_{11}$  is generally below  $-30$  dB, indicating a very good coupling from the feeding  $TE_{11}$  mode to the electromagnetic crystal waveguide modes. Once the S-parameters were obtained, the waveguide power loss factor was calculated by the following equation:

$$\alpha = \ln\left(\frac{|S_{21}|^2}{1 - |S_{11}|^2}\right) / (-l), \quad (1)$$

where  $l$  is the waveguide length.

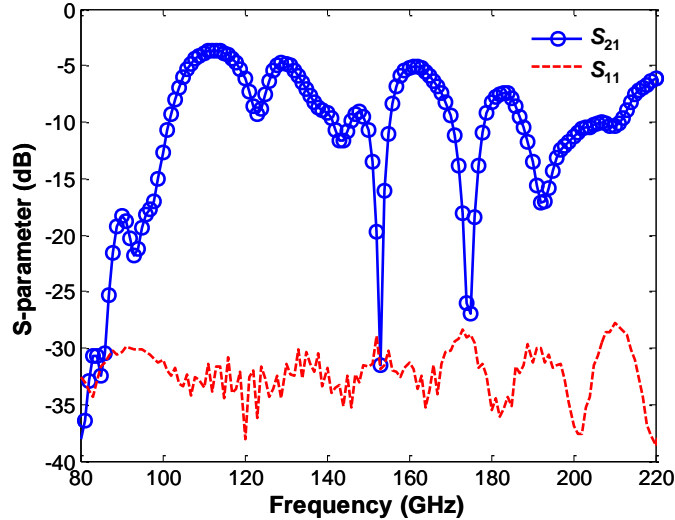


Fig. 2. Simulated S-parameters of an 84 mm-long electromagnetic crystal waveguide.

In a practical experiment, circular metallic waveguide feeds would be inconvenient due to cost and issues in calibrating their losses. Instead, quasi-optical measurement with an incident THz Gaussian beam is preferred. The second simulation is carried out accordingly. In this case, a Gaussian beam of 3-mm beam waist was aimed at the electromagnetic crystal waveguide aperture, and the power flux transmitted out of the other end of the waveguide was calculated. The power flux calculation was performed by integrating the Poynting vector component along the longitudinal direction,  $S_z$ , over a surface covering the cross-sectional area of the waveguide. Since the coupling coefficients at the incidence and output ends are identical and independent of the waveguide length, the transmitted power flux has an exponentially decaying relation with waveguide length. A semi-log plot of the transmitted power flux (in dB) versus waveguide length should then be a straight line with a negative slope, which is the intrinsic power loss factor of the waveguide.

This conclusion only holds, however, when multiple reflections within the waveguide are excluded either via time-gating or have negligible magnitudes. Time-domain gating is in principle not quite suitable for electromagnetic crystal waveguide, because it is a highly dispersive system with narrow band features. Its time-domain responses therefore decay very slowly indicating that the multiple reflections mix together, making isolation difficult. However, the assumption that multiple reflections are of negligible magnitude is likely true in our case, as the energy is incident from free space into the air core, and couples to the waveguide propagation modes with an effective refractive index very close to 1 according to Lumerical MODE simulation.

Four waveguides of lengths of 100, 110, 120 and 130 mm were simulated under the same Gaussian beam excitation, and the transmitted power flux in the passbands does indeed show the expected exponential decay as the waveguide length increases. The extracted waveguide loss using these two simulation methods are compared in Fig. 3. The two loss spectra show very good consistency in terms of frequency and depth of the low-loss bands. The lowest propagation loss obtained is 0.022 dB/mm at 112 GHz, which corresponds to a quality ( $Q$ ) factor of 463 obtained from the formula  $Q = \beta/(2\alpha')$ , where  $\beta$  is the wave number and  $\alpha' = \alpha/2$  is the field attenuation constant, both in linear units. Therefore, the material loss and potential losses from higher-order modes bring in an extra of 0.01 dB/mm loss at this frequency, when compared to the eigen-mode simulation result of the fundamental  $HE_{11}$  mode in the last section. Although 5 periods of the cladding lattice was used in the design and practically fabricated later on, simulation proves that 3 periods are adequate to achieve almost identical low-loss propagation.

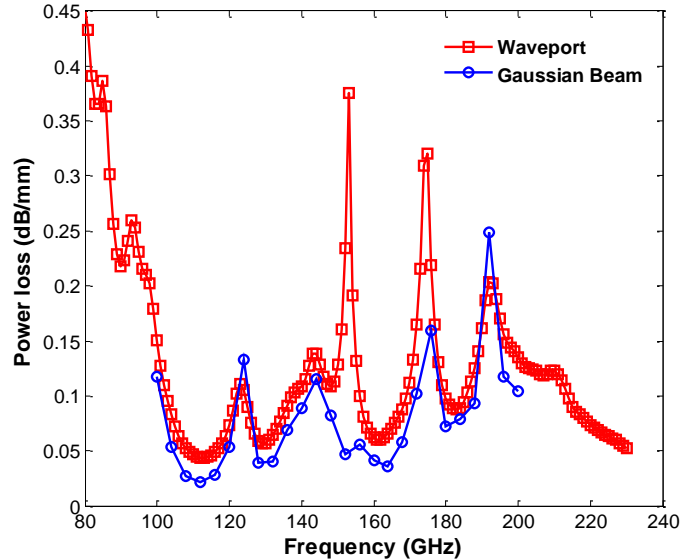


Fig. 3. Power loss factors of the electromagnetic crystal waveguide extracted from the wave port ( $TE_{11}$  circular perfect-electric-conductor waveguide feeds) and the Gaussian beam incidence simulations.

#### 4. Experiment

Fabrication of the waveguide was carried out by the aforementioned polymer jetting technique. The structure was printed vertically along the wave channel direction. In this fabrication, the glossy mode with reduced support material usage was applied to minimize surface roughness, as only limited support structure was needed. Figure 4 shows photos of the cross-sectional and full view of a fabricated waveguide.

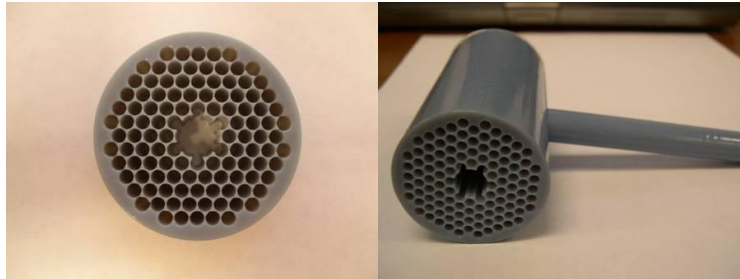


Fig. 4. Cross-sectional and full views of a fabricated THz waveguide, with lattice constant of 3 mm, center core radius of 4.2 mm, and cladding air cylinder radius of 1.3 mm.

A THz time-domain spectroscopy (THz-TDS) system with photoconductive antennas as transmitter and receiver [34] was used for the waveguide characterization. The antennas were able to produce usable spectral content from 50 GHz to 1.2 THz with a peak around 100 GHz. Two off-axis parabolic mirrors with 152.4 mm effective focal length were used to focus the incident beam from the transmitter to a 5.4 mm beam waist. In order to efficiently convert the incident Gaussian beam to the desired  $HE_{11}$  waveguide mode, their electric field profiles needed to be well-matched [32]. According to a modal field overlap calculation [32], an optimum beam waist of 2.7 mm would couple the incident Gaussian beam to the waveguide  $HE_{11}$  mode with over 90% efficiency. Therefore, a plano-convex polymer lens pair was designed and fabricated by the same rapid prototyping method and used to further focus the beam to the desired size. When placed at the focal point of the off-axis parabolic mirror, the lens focuses the beam to a 2.7 mm waist verified by a razor-blade measurement.

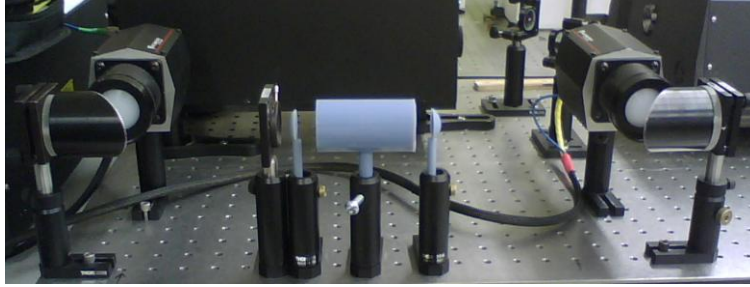


Fig. 5. Setup of the characterization experiment: from left to right: THz transmitter, parabolic mirror 1, iris, polymer lens 1, waveguide under test, polymer lens 2, parabolic mirror 2, and THz receiver. THz time-domain spectrometer used here: T-Ray 2000 turnkey THz system manufactured by Picometrix, Inc.

Figure 5 shows a photo of the quasi-optic setup for waveguide characterization. The iris in the photo was only for the purpose of marking the beam position and opens sufficiently for the entire beam to pass through unobstructed. As discussed previously, waveguides of several lengths needed to be measured in order to characterize the propagation loss factor, similar to the “cut-back” method used in optical fiber loss measurement [35]. Therefore, the spacing between all elements and the waveguide ends were kept the same throughout the measurements to provide an identical optical path with the exception of the waveguide section.

Five waveguides of lengths 50, 75, 100, 125, and 150 mm and identical cross section were placed in the beam path sequentially, and their transmitted waveforms were measured. The two lenses were also positioned 35 mm (17.5 mm x 2) away without a waveguide in between to obtain a reference scan. The spectrometer was set to operate in the long scan mode, covering the entire available time delay range of 1200 pico-second (ps) with a scan speed of 5 ps per second. Each recorded scan was an average of five consecutive scans. The resulted waveforms are shown in Fig. 6(a). The reference scan leads in time, followed by the five waveguide scans with increased delays from the longer waveguides. Dispersion with respect to the reference waveform is observed in all five waveguide scans, which is a clear sign of guided mode resonances. Figure 6(b) plots the power transmittances of all the waveguides, which were obtained by Fourier transforming the waveforms to the frequency domain, then normalizing the spectra with respect to the reference spectrum. Four passbands centered around 105, 123, 153 and 174 GHz can be clearly seen, corresponding to the four passbands in Fig. 2 to within a downshift of a few GHz.

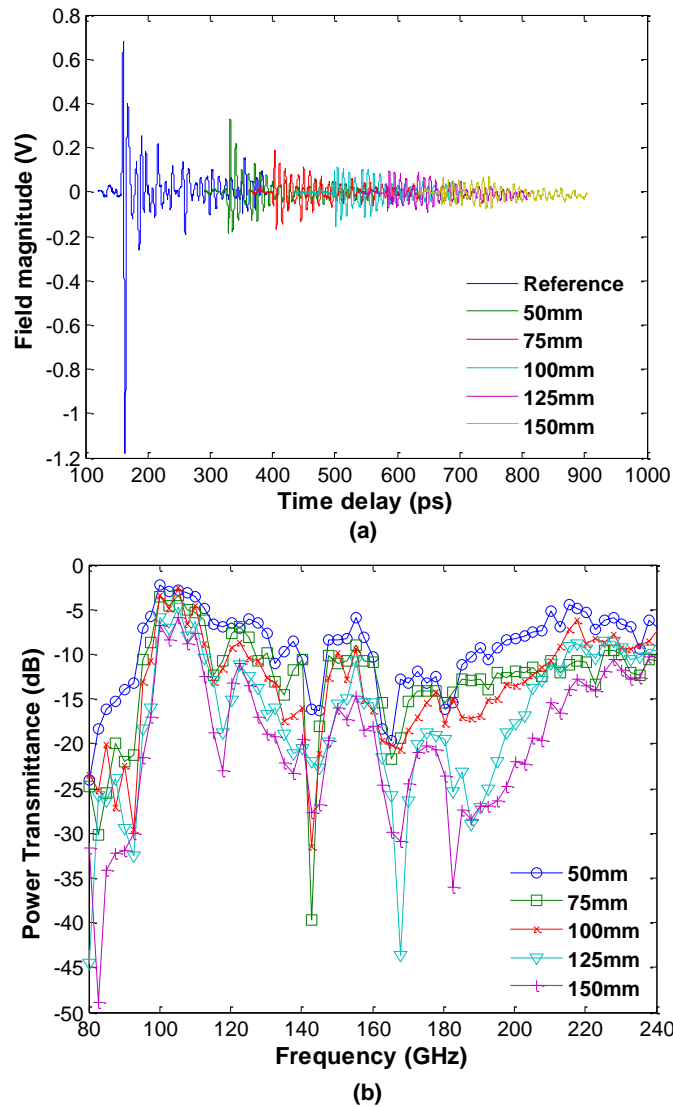


Fig. 6. (a) Transmitted waveforms of five waveguides with different lengths, and the reference scan transmitted through free space. (b) Normalized power transmission of the waveguides.

Extraction of the waveguide power loss factor was implemented through the same linear-fit process as described in the previous section. Figure 7(a) plots the relative transmission power at 107 GHz, which is the center frequency of the first passband. Except for a slight deviation from a straight line at the 100 mm length, the transmitted power in dB decreases linearly as the waveguide length increases. The slope of 0.056 dB/mm is the measured waveguide power loss factor at this frequency. It is worth mentioning that time spans of the truncated waveforms utilized in Fig. 6 were short enough so that it was guaranteed no multiple reflections were included in the calculations. The truncation, however, did use sufficiently-long waveforms so that majority of the transmitted power is retained in the calculation.

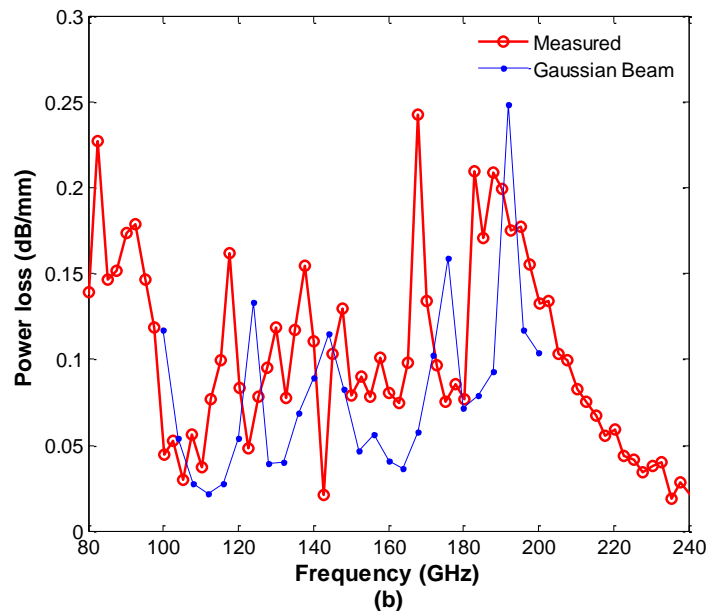
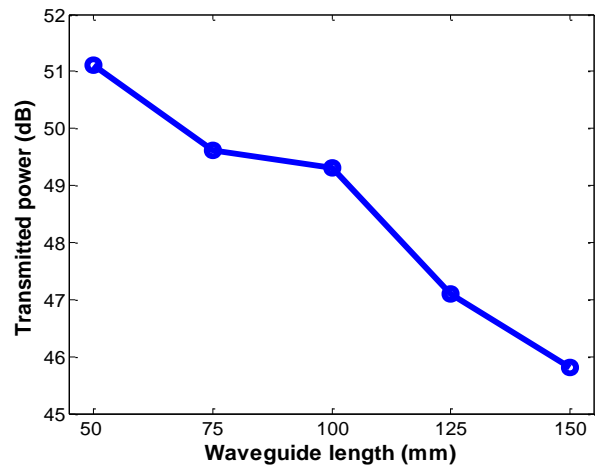


Fig. 7. (a) Semi-log plot of the measured transmitted power in dB versus waveguide length at 107 GHz. Linearly fitted slope gives the power loss factor at this frequency. (b) Measured and simulated waveguide power loss factors under Gaussian beam excitation.

As shown in Fig. 7(b), the measured power loss factors agree quite well with the beam-incidence simulation results. The measured 7-GHz downshift is possibly due to fabrication tolerance, as the air cylinder diameter may not be precisely controlled due to the reduced support material usage in the glossy fabrication mode. Further, the model material has slight dielectric constant dispersion (from 2.8 to 2.73) within the 100-150 GHz range [19], which was not included in the simulations and would also contribute to the discrepancy. Note that the dip at 143 GHz is not reliable because as it is at a deep band-stop frequency (as shown in Fig. 6(b)) for which the signal-to-noise-ratio is not good. Nevertheless, the measurement and the simulation agree well, demonstrating four passbands with low propagation losses at nearby frequencies. The lowest observed power loss factor was 0.03 dB/mm at 105.2 GHz, corresponding to a  $Q$  factor of 319 at this frequency. As a reference, a standard W-band rectangular waveguide (WR-10, 75-110 GHz) made of copper has a theoretical power attenuation factor of 0.0023-0.0035 dB/mm. However, the practically measured W-band

rectangular waveguide loss reaches 0.01-0.015 dB/mm in [16] and even 0.05-0.07 dB/mm in [17], which are 5 ~ 20 times of the theoretical value. Other reported THz micro-structured waveguides working at similar frequency regime include the sub-wavelength porous fiber by Dupuis *et al.* in [10], hollow-core photonic crystal fiber by Nielson *et al.* in [13], solid-core PCF by Goto *et al.* in [12], etc. The porous fiber demonstrated a very low power loss factor of 0.004 dB/mm at 300 GHz, whereas the solid-core PCF reported a ~0.05 dB/mm loss factor mainly due to material loss. THz micro-porous guidance was claimed to be observed at 200 GHz in [13], however the loss value was not reported. While certainly not presenting the lowest loss coefficient for waveguides at 100 – 300 GHz range, the waveguide reported in this work finds its own advantage in the ease and flexibility of the fabrication process. Moreover, with optimized polymer materials, lower loss should be achieved.

## 5. Conclusion

A THz waveguide based on a hollow-core electromagnetic crystal structure was designed and then fabricated by polymer jetting rapid prototyping. Quasi-optical THz lenses were also fabricated by the same technique in help with mode-matching the waveguide to free-space Gaussian beams. Results of the power loss factor characterization showed good agreement with simulation. A low transmission loss waveguide operating near 105 GHz was demonstrated with minimal fabrication complexity and cost. Scaling the waveguide to a few hundreds of GHz is feasible under the scope of this fabrication method, and is currently pursued in our lab. Because of the systematic fabrication manor of the rapid prototyping technique, this waveguide can be readily integrated with other THz components such as electromagnetic crystal based horn antennas, THz planar circuits (so that semiconductor based THz source and detector can be readily integrated), and other quasi-optical parts fabricated by the same approach. We anticipate that this will ultimately lead to integrated fully-functional THz systems.

## Acknowledgments

This work was supported in part by the National Science Foundation under Awards 0823864 and 0925220, and the state of Arizona under TRIF.